Gyrokinetic turbulent transport simulation of a high ion temperature plasma in large helical device experiment

M. Nunami, T.-H. Watanabe, H. Sugama, and K. Tanaka

Related Articles

A link between nonlinear self-organization and dissipation in drift-wave turbulence
Phys. Plasmas 19, 082318 (2012)

Nonlinear instability saturation due to quasi-particle trapping in a turbulent plasma
Phys. Plasmas 19, 082316 (2012)

The nonlinear dispersion relation of geodesic acoustic modes
Phys. Plasmas 19, 082315 (2012)

On apparent temperature in low-frequency Alfvénic turbulence
Phys. Plasmas 19, 084504 (2012)

Scale coupling in Richtmyer-Meshkov flows induced by strong shocks
Phys. Plasmas 19, 082706 (2012)

Additional information on Phys. Plasmas

Journal Homepage: http://pop.aip.org/

Journal Information: http://pop.aip.org/about/about_the_journal

Top downloads: http://pop.aip.org/features/most_downloaded

Information for Authors: http://pop.aip.org/authors

Gyrokinetic turbulent transport simulation of a high ion temperature plasma in large helical device experiment

M. Nunami,[1,a)] T.-H. Watanabe,[1,2] H. Sugama,[1,2] and K. Tanaka[1]
[1]*National Institute for Fusion Science, Toki, Gifu 509-5292, Japan*
[2]*The Graduate University for Advanced Studies, Toki, Gifu 509-5292, Japan*

Ion temperature gradient turbulent transport in the large helical device (LHD) is investigated by means of gyrokinetic simulations in comparison with the experimental density fluctuation measurements of ion-scale turbulence. The local gyrokinetic Vlasov simulations are carried out incorporating full geometrical effects of the LHD configuration, and reproduce the turbulent transport levels comparable to the experimental results. Reasonable agreements are also found in the poloidal wavenumber spectra of the density fluctuations obtained from the simulation and the experiment. Numerical analysis of the spectra of the turbulent potential fluctuations on the two-dimensional wavenumber space perpendicular to the magnetic field clarifies the spectral transfer into a high radial wavenumber region which correlates with the regulation of the turbulent transport due to the zonal flows. The resultant transport levels at different flux surfaces are expressed in terms of a simple linear relation between the transport coefficient and the ratio of the squared turbulent potential fluctuation to the averaged zonal flow amplitude. © *2012 American Institute of Physics*. [http://dx.doi.org/10.1063/1.4704568]

I. INTRODUCTION

Helical systems such as stellarators and heliotrons[1] are considered to be one of the promising concepts for the magnetic confinement fusion reactor, because they are advantageous in realizing long-time discharges without external current drives. In addition to the issue of the confinement field optimization for decreasing the neoclassical transport,[2] reduction of the anomalous transport, which is caused by the plasma turbulence, is another critical issue for improving confinement properties of helical plasmas.[3,4] Furthermore, the anomalous transport phenomena make significant roles not only in fusion plasmas but also in more general fields, e.g., astrophysics, space physics, and laboratory plasmas,[5] as the turbulence is ubiquitously found in the nature. Nowadays, it has been considered that plasma turbulence is determined by the interaction between the microinstabilities such as ion temperature gradient (ITG) modes and zonal flows.[6,7] To understand the transport physics, we need to study not only ideal and simplified models, but also the concrete experimental results observed in real systems. In recent years, gyrokinetic simulations have been extensively done to investigate turbulent transport processes in tokamaks[8,9] and helical systems.[3,4,10,11] While there are several publications on validation of the gyrokinetic turbulent transport simulations in tokamaks (for example, Ref. 12), no direct comparison between gyrokinetic simulations and the experimental data of helical systems has been reported so far. The present study constitutes the first attempt to compare the gyrokinetic simulations of ITG turbulence with the experimental observations in the Large Helical Device (LHD)[13] experiment by elaborately adopting the three-dimensional equilibrium recon-

structed from experimental data for the high ion temperature discharge of shot number 88343.[14,15]

This paper is organized as follows. In Sec. II, we briefly describe the simulation model used in the present study and basic equations employed in the calculation. In Sec. III, we show the ITG turbulence simulation results and perform the comparisons between the simulation and the LHD experiment. Also, in the section, we discuss the spectral transfer of the potential fluctuations which leads reduction of the transport, and relation between the resultant transport levels, turbulent fluctuation, and zonal flow amplitude. Finally, we summarize the work in Sec. IV.

II. SIMULATION MODEL

In our previous paper,[16] we performed the linear gyrokinetic simulations for ITG instability in the LHD high ion temperature discharge #88343 [see Fig. 2(a) for the radial profiles of the ion temperature and the electron density], where we found that the density fluctuations measured by phase contrast imaging (PCI) method in the LHD discharge have large amplitudes for the radial regions which correspond to ITG modes having large growth rates. In the present work, applying the gyrokinetic Vlasov flux-tube code GKV-X,[17] we perform the nonlinear ITG turbulent transport simulations to evaluate the saturation levels of the turbulent fluctuations, zonal flows, and ion heat transport in the LHD discharge.

As shown in Ref. 17, the GKV-X incorporates large number of Fourier components of the magnetic field as well as full geometrical information of the flux surfaces by using VMEC code[18] for the three-dimensional MHD equilibrium configuration corresponding to experimental profiles of the plasmas. The GKV-X solves the nonlinear gyrokinetic equation[19,20] for the ion perturbed gyrocenter distribution function δf with the mass m_i in the low-β electrostatic limit,

a)Electronic mail: nunami.masanori@nifs.ac.jp.

$$\left(\frac{\partial}{\partial t} + v_{\parallel}\boldsymbol{b}\cdot\nabla + \frac{c}{B}\boldsymbol{b}\times\nabla\Phi\cdot\nabla - \frac{\mu}{m_{\mathrm{i}}}\boldsymbol{b}\cdot\nabla B\frac{\partial}{\partial v_{\parallel}} + \boldsymbol{v}_{\mathrm{d}}\cdot\nabla\right)\delta f$$

$$= (\boldsymbol{v}_{*} - \boldsymbol{v}_{\mathrm{d}} - v_{\parallel}\boldsymbol{b})\cdot\frac{e\nabla\Phi}{T_{\mathrm{i}}}F_{\mathrm{M}} + C(\delta f), \qquad (1)$$

where $v_{\parallel}$ and $\mu = m_{\mathrm{i}}v_{\perp}^{2}/2B$ are the parallel velocity and the magnetic moment, respectively, which are employed as the velocity-space coordinates. F_{M} is the Maxwellian distribution with the temperature T_{i}, and $\boldsymbol{b} = \boldsymbol{B}/B$ is the parallel unit vector. The magnetic and diamagnetic drift velocities are defined by $\boldsymbol{v}_{\mathrm{d}} = (c/eB)\boldsymbol{b}\times(\mu\nabla B + m_{\mathrm{i}}v_{\parallel}^{2}\boldsymbol{b}\cdot\nabla\boldsymbol{b})$ and $\boldsymbol{v}_{*} = (cT_{\mathrm{i}}/eB)\boldsymbol{b}$ $\times[\nabla\ln n + (m_{\mathrm{i}}v^{2}/2T_{\mathrm{i}} - 3/2)\nabla\ln T_{\mathrm{i}}]$, respectively. In the GKV-X, the local flux-tube model[21] is used with the field-aligned coordinates $\{x, y, z\}$ which are related with the Boozer coordinates[22] $\{r, \theta, \zeta\}$ with radial coordinate r, poloidal angle θ, and toroidal angle ζ, as $\{x, y, z\} = \{r - r_{0}, (r_{0}/q_{0})$ $[q(r)\theta - \zeta], \theta\}$ around the flux surface at r_{0}. Here, $q(r)$ is the safety factor at r, and $q_{0} = q(r_{0})$. The coordinate $z = \theta$ is defined along the field line labeled by $\alpha = \zeta - q_{0}\theta$ = constant. The same collision term $C(\delta f)$ as in Ref. 10 is employed. In the wavenumber space (k_{x}, k_{y}), the gyro-phase averaged electrostatic potential at the gyrocenter position Φ is related to that at the particle position ϕ as $\Phi_{k_{x},k_{y}} = J_{0}(k_{\perp}v_{\perp}/\Omega_{\mathrm{i}})\phi_{k_{x},k_{y}}$. Here, $J_{0}(k_{\perp}v_{\perp}/\Omega_{\mathrm{i}})$ is the zeroth-order Bessel function which represents the finite gyroradius effect. Employing the quasi-neutrality condition, $\phi_{k_{x},k_{y}}$ is calculated by

$$\int d^{3}v J_{0}\delta f_{k_{x},k_{y}} - n_{0}\frac{e\phi_{k_{x},k_{y}}}{T_{\mathrm{i}}}[1 - \Gamma_{0}(b_{k})] = \delta n_{\mathrm{e},k_{x},k_{y}}, \qquad (2)$$

where $\delta f_{k_{x},k_{y}}$ is the Fourier component of δf, n_{0} is the averaged electron density, $\Gamma_{0}(b_{k}) = I_{0}(b_{k})\exp(-b_{k})$ with $b_{k} = (k_{\perp}v_{\mathrm{ti}}/\Omega_{\mathrm{i}})^{2}$, and I_{0} is the zeroth-order modified Bessel function. The electron density perturbation $\delta n_{\mathrm{e},k_{x},k_{y}}$ is assumed to be given in terms of the potential by

$$\frac{\delta n_{\mathrm{e},k_{x},k_{y}}}{n_{0}} = \begin{cases} [\phi_{k_{x},k_{y}} - \langle\phi_{k_{x},k_{y}}\rangle]/T_{\mathrm{e}} & \text{if } k_{y} = 0, \\ e\phi_{k_{x},k_{y}}/T_{\mathrm{e}} & \text{if } k_{y} \neq 0, \end{cases} \qquad (3)$$

where T_{e}, n_{0}, and $\langle\cdots\rangle$ represent the electron temperature, the background density, and the flux surface average, respectively. Here, only pure ITG modes are treated by using the adiabatic electron response for $k_{y} \neq 0$, and we do not consider

trapped electron modes (TEMs) which are considered to be stable in the flattened density profile shown in Fig. 2(a).

III. ITG TURBULENCE SIMULATION FOR LHD HIGH-T_{i} DISCHARGE

The nonlinear flux-tube ITG turbulence simulations are performed in the LHD discharge #88343 at different radial positions, $\rho = 0.46, 0.65$ and 0.83, independently. Here, $\rho \equiv \sqrt{\Psi/\Psi_{a}}$ is the normalized minor radius with the toroidal magnetic flux $\Psi = B_{\mathrm{ax}}r^{2}/2$ at the minor radius r, and Ψ_{a} at the last closed surface $r = a$. Here, B_{ax} is the field strength at the magnetic axis. The experimental results show that $T_{\mathrm{i}}/T_{\mathrm{e}} = 1$ is well satisfied for these radial positions,[15] and we assume $n_{\mathrm{i}}/n_{\mathrm{e}} = 1$. The simulation conditions, such as gradient scale lengths of the ion temperature $L_{T\mathrm{i}}$ and density L_{n}, are the same as in previous linear simulations[16] except for the incorporation of the nonlinear term and the collisional effect. The used collision frequency $\nu = 0.00225 v_{\mathrm{ti}}/R_{0}$ is so small that its effect on the dispersion relation of the ITG instability is negligible. Here, R_{0} is the major radius of the torus. For the ITG turbulence simulation in the helical systems which have complicated magnetic field structures, high resolution along the field line is necessary. Therefore, we used a huge number of the grid points in the five dimensional phase space, $128 \times 128 \times 512 \times 128 \times 48$ in the $(x, y, z, v_{\parallel}, \mu)$-space. The simulation box size in the velocity space $(v_{\parallel}, \mu)$ is $-5v_{\mathrm{ti}} \leq v_{\parallel} \leq 5v_{\mathrm{ti}}$ and $0 \leq \mu \leq 12.5 m_{\mathrm{i}}v_{\mathrm{ti}}^{2}/B_{0}$, where $\mu = m_{\mathrm{i}}v_{\perp}^{2}/2B_{0}$ is the magnetic moment and $B_{0} = B_{00}(\rho)$ is the Fourier component of the field with the poloidal and toroidal mode number $(m, n) = (0, 0)$. In the real space, we use $-\pi \leq z < \pi$ along the field line direction, and the system lengths in perpendicular directions are $L_{x} = 2\pi/\Delta k_{x}$ and $L_{y} = 2\pi/\Delta k_{y}$, where $(\Delta k_{x}, \Delta k_{y})$ are minimum wavenumbers in (x, y)-space given by $(\Delta k_{x}\rho_{\mathrm{ti}}, \Delta k_{y}\rho_{\mathrm{ti}}) = (0.116, 0.035), (0.128, 0.038)$, and $(0.122, 0.042)$ for $\rho = 0.46, 0.65$, and 0.83, respectively, where $\rho_{\mathrm{ti}} \equiv v_{\mathrm{ti}}/(eB_{0}/m_{\mathrm{i}}c)$ is the ion thermal gyroradius with the thermal speed $v_{\mathrm{ti}} = \sqrt{T_{\mathrm{i}}/m_{\mathrm{i}}}$.

A. Comparison with the LHD experiment

Figure 1 shows snapshots of the perturbed electrostatic potentials obtained from the simulations at each flux surface in linear phase of the ITG mode growths and in nonlinear saturated phase. We perform comparison of the ion transport
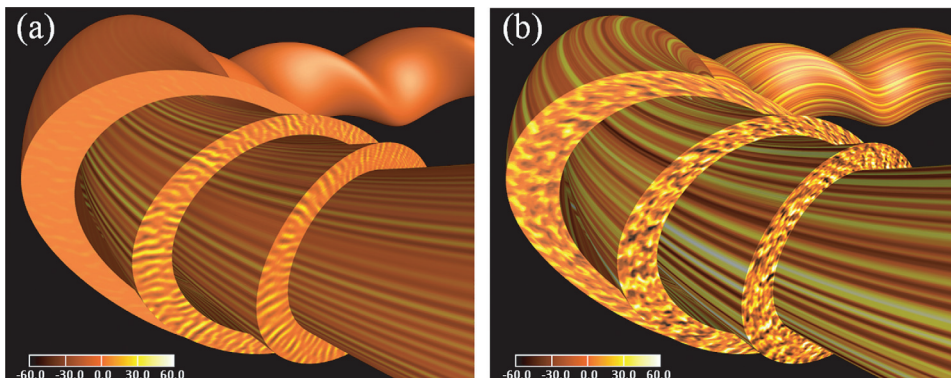

FIG. 1. Snapshots of the perturbed electrostatic potentials ϕ obtained from GKV-X simulations at $\rho = 0.46, 0.65$ and 0.83 in the LHD high-T_{i} discharge for (a) linear phase $(t \sim 18R_{0}/v_{\mathrm{ti}}^{(\rho=0.65)})$ and (b) nonlinear saturated phase $(t \sim 60R_{0}/v_{\mathrm{ti}}^{(\rho=0.65)})$. The value of ϕ is normalized by $T_{i}^{(\rho=0.65)}$ $\rho_{\mathrm{ti}}^{(\rho=0.65)}/eR_{0} \sim 1.06 \times 10^{-3}$[kV], where $T_{i}^{(\rho=0.65)} \sim 2.2$[keV], $v_{\mathrm{ti}}^{(\rho=0.65)} \sim 4.6 \times 10^{5}$ [m/s], $\rho_{\mathrm{ti}}^{(\rho=0.65)} \sim 1.8 \times 10^{-3}$[m], and $R_{0} \sim 3.75$[m].
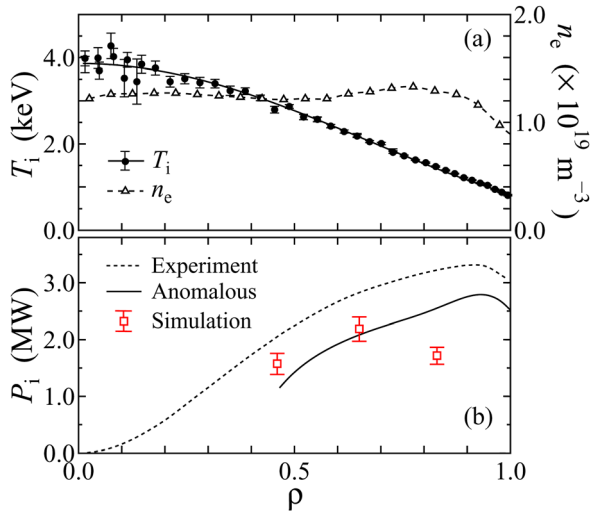
FIG. 2. Radial profiles of (a) the ion temperature T_i, electron density n_e in the LHD experiment #88343, and (b) ion heat flux P_i obtained from the experiment (dotted curve) and the GKV-X simulations (open squares with the error bars). The solid curve in (b) represents the anomalous part of the experimental P_i.

TABLE I. The ion heat diffusivity from the anomalous contribution given by the LHD experiment and from the ITG turbulent transport obtained from the GKV-X simulations in physical unit $\chi_i[m^2/s]$, and the gyro-Bohm unit $\chi_i/(\rho_{ti}^2 v_{ti}/R_0)$, where $\rho_{ti} = v_{ti}/(eB_0/m_i c)$ and $v_{ti} = \sqrt{T_i/m_i}$.

ρ		0.46	0.65	0.83
$\chi_i[m^2/s]$	Experiment	2.40	2.71	2.73
	Simulation	3.60	2.84	1.84
$\chi_i/(\rho_{ti}^2 v_{ti}/R_0)$	Experiment	3.85	6.63	11.59
	Simulation	5.79	6.97	7.80

part of P_i, such that the observed differences are less than 10% for $\rho = 0.46, 0.65$, and about 30% for $\rho = 0.83$ (see also Table I for the ion heat diffusivity χ_i).

Figure 3 shows the poloidal wavenumber spectra of the turbulent density fluctuation obtained from the PCI measurement and the simulation, where k_y is treated as the poloidal wavenumber in the coordinates used in the simulation. The both spectra have a peak in a low wavenumber region of $k\rho_{ti} < 0.5$ and similar shape in a high wavenumber region of $k\rho_{ti} > 0.5$, although the peak position of the experimental spectrum is found at a higher wavenumber than that obtained from the simulation. It should be remarked that, because of coarse resolution and the cutoff of the wavenumber at $k_\theta \rho_{ti} \sim 0.4$ in the PCI measurement, the experimental results in lower wavenumber region have a large ambiguity. Of course, contributions of kinetic electrons, which are not taken into account in the GKV-X code, should be considered for more precise analyses. We still need to improve the simulation code for treating kinetic electrons although we can expect that the ITG turbulences shown by the simulations here give a dominant contribution to the transport for the present case with the flattened density profile in Fig. 2(a). The reasonable agreements between the LHD high ion temperature experiments and the ITG turbulence simulations by GKV-X strongly encourage us to pursue further gyrokinetic simulation studies of the anomalous transport in non-axisymmetric systems.

B. Spectral transfer of potential fluctuations

It is now widely recognized that the ITG turbulent transport is determined by the competitive interaction between turbulence and zonal flows, and there have been a number of theoretical studies which investigate effects of magnetic

level resulting from the simulation with the LHD experimental observation for the first time.

In the saturation phase of the turbulence, we evaluate the time-averaged ion heat flux through each flux surface $P_i(\rho)$ defined by integrating the ion heat flux density $Q_i(\rho)$ over the flux surface as $P_i(\rho) = \int Q_i(\rho)dS(\rho)$ for each radial position. Here, $dS(\rho)$ is areal element at the flux surface with ρ. Note that the experimental profile of the electron density in the LHD experiment #88343 shown in Fig. 2(a) is so flattened for $\rho < 0.9$ that the trapped electron modes, which are not included in the present model, are considered to be stable and have no contributions to the turbulent transport. Figure 2(b) shows the profile of the ion heat fluxes P_i obtained from the GKV-X simulations and from the experiment. The error bars for the simulation results are evaluated from the errors of the ion temperature gradient scale length $L_{Ti} \equiv -(d\ln T_i/dr)^{-1}$ obtained from the experimental observation of the ion temperature profile in Fig. 2(a). The simulation results are 15%–50% lower than that in the experimental values which include both the anomalous and neoclassical contributions to the transport. If we subtract the neoclassical part calculated by the GSRAKE code,[23] the simulation results agree well with the anomalous
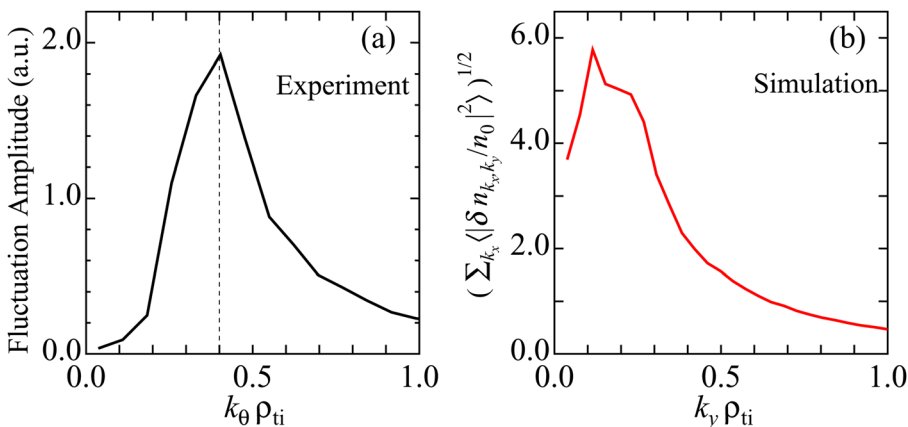

FIG. 3. Poloidal wavenumber spectra for the density fluctuation amplitude obtained from (a) the PCI measurement for $\rho = 0.6 - 0.7$ in the LHD experiment, and (b) the GKV-X simulations at $\rho = 0.65$. In (a), the dashed line represents the cutoff of the wavenumber in the PCI measurement. The ordinate of (b) is normalized by R_0/ρ_{ti}.
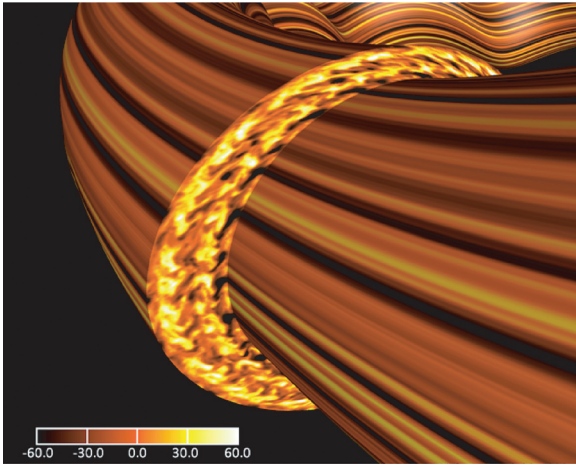
FIG. 4. Snapshot of the perturbed electrostatic potential ϕ obtained from GKV-X simulations at $\rho = 0.65$ in the turbulent state for the vacuum field configuration. For normalization of ϕ, the same numerical factor as Fig. 1 is used.

geometry on zonal flows and turbulence in helical systems.[24–27] Figure 5(a) shows the power spectra of the turbulent potential fluctuations in the k_y space normalized by gyro-Bohm unit $T_i \rho_{ti}/e R_0$, which are obtained by integrating the squared potential fluctuations over the k_x space $\sum_{k_x} \langle |e\phi_{k_x,k_y} R_0 / T_i \rho_{ti}|^2 \rangle / \Delta k_y$, and taking the time averages in the saturated phases for three simulation runs at each radial position. In the plots, we also show the simulation result obtained by using the vacuum (or zero beta) magnetic field configuration at $\rho = 0.65$, where the same simulation parameters of the experiment #88343 at $\rho = 0.65$ are used except for the field configuration and the values of minimum wavenumbers $(\Delta k_x \rho_{ti}, \Delta k_y \rho_{ti}) = (0.126, 0.036)$. In this vacuum field configuration with no Shafranov shift, the magnetic axis is more inward shifted, the neoclassical transport is lower, and the zonal flow response is better than in the configuration of the experiment as theoretically expected.[24] The potential fluctuation at $\rho = 0.65$ in the turbulent state for the vacuum field configuration is shown in Fig. 4, where the zonal flow structure is seen more clearly than in the $\rho = 0.65$ case of Fig. 1(b). In the experimental configuration, the spectrum at $\rho = 0.83$ has a peak in a lower region of k_y than those at inner radial positions. The peak amplitude of the fluctuation spectrum at $\rho = 0.83$ in the gyro-Bohm unit is about 5 times higher than that in $\rho = 0.65$ case, and 10 times higher than in $\rho = 0.46$ case. We also find that the peak amplitude in the inward-shifted configuration is larger than in the experimental

one. According to the mixing length estimate,[28] the turbulent transport is roughly characterized by γ/k_y^2, where γ is the linear growth rate of the mode. For the cases corresponding to those in Fig. 5(a), we plot spectra of γ/k_y^2 in Fig. 5(b), where one finds obvious differences in the low k_y region of $k_y \rho_{ti} < 0.2$–0.3. The peak value of γ/k_y^2 at $\rho = 0.83$ is 5–10 times higher than the other radial positions in the experimental cases. At $\rho = 0.65$, γ/k_y^2 for the inward-shifted case is higher than that for the experimental case. The peak position shifts to the lower k_y side for the outer radial position in similar to the power spectrum of potential fluctuations in Fig. 5(a). Thus, the turbulence spectra are correlated with the mixing length estimate although it is not simply concluded that mixing length estimate from the linear growth rate solely influences the turbulent transport level, because the interaction between zonal flow and turbulence is also a key ingredient determining the transport.

In Fig. 6, the two-dimensional spectra of the squared potential fluctuations in the wavenumber space (k_x, k_y) are shown. Spectra for the experimental case with $\rho = 0.83$ and inward-shifted case clearly spread in the high-k_x region which is caused by the spectral transfer from the low-k_x to the high-k_x space. The ITG mode is linearly less-unstable in the high-k_x region as seen in Fig. 7(a) where the two-dimensional growth rate spectrum in the inward-shifted case is shown. The two-dimensional potential fluctuation spectrum shown in Fig. 6 for the inward-shifted case is magnified and plotted in Fig. 7(b). The zonal flow generation is identified as a bright-colored horizontal stripe at $k_y = 0$ in Fig. 7(b) more clear than in Fig. 6. It is found by comparing Figs. 7(a) and 7(b) that the fluctuation spectrum widely invades the less-unstable high-k_x region and the fluctuation peak is located at the k_y lower than the one corresponding to the maximum growth rate. The spectral transfer is considered to be induced through the interaction between zonal flows and turbulence as discussed in Ref. 29. The high-k_x modes in the spreading spectrum make less contribution to the transport while they still contribute to the integrated power spectrum shown in Fig. 5(a). Indeed, as shown in Fig. 8(a) for the spectra of the squared zonal flow potential $\langle |e\phi_{k_x,0} R_0 / T_i \rho_{ti}|^2 \rangle / \Delta k_x$, larger zonal flows causing the spectrum spreading are generated for $\rho = 0.83$ and inward-shifted cases. Linear simulation results of the response of the zonal flow potential to an initially given source are shown in Fig. 8(b). It is found from Figs. 8(a) and 8(b) that the linear zonal flow response has a positive correlation with the amplitude of the zonal flow potential in the turbulent state.
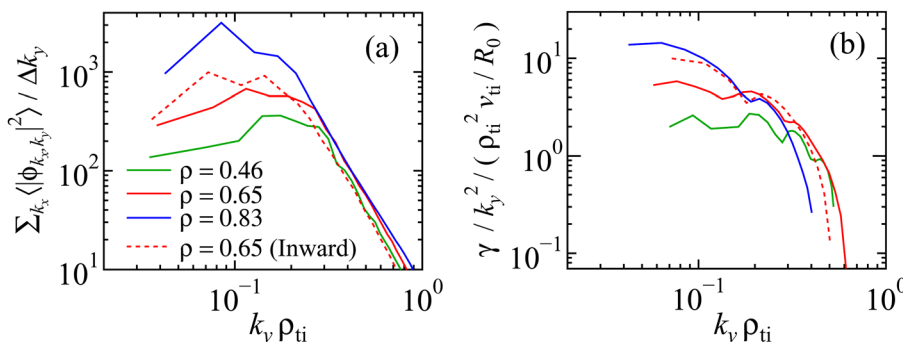

FIG. 5. Spectra of (a) time-average of squared potential fluctuations in k_y space integrated over k_x space, and (b) linear ITG growth rates divided by square of the wavenumber k_y, at $\rho = 0.46$, 0.65, and 0.83 in the experimental case, and at $\rho = 0.65$ in the inward-shifted vacuum configuration case. In (a), ϕ and Δk_y are normalized by $T_i \rho_{ti}/e R_0$ and ρ_{ti}^{-1}, respectively.
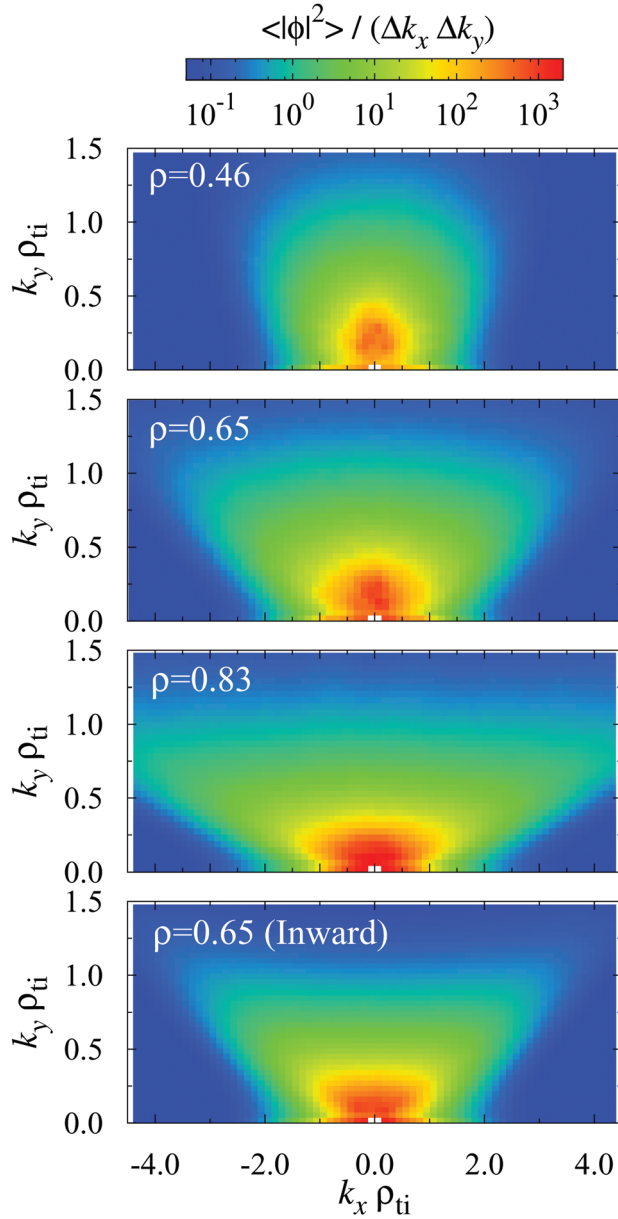
FIG. 6. Spectra of time-averaged potential fluctuations in (k_x, k_y) space at $\rho = 0.46$, 0.65, and 0.83 in the experimental case, and at $\rho = 0.65$ in the inward-shifted case. Here, ϕ and $(\Delta k_x, \Delta k_y)$ are normalized by $T_i \rho_{ti}/eR_0$ and ρ_{ti}^{-1}, respectively.

C. Resultant transport level

Correlations of the resultant transport level on the turbulence and the zonal flow are examined in the Lissajous plots in Fig. 9 for the squared turbulent potential,

$$\mathcal{T} \equiv \frac{1}{2} \sum_{k_x, k_y \neq 0} \left\langle \left| \frac{e\phi_{k_x,k_y}R_0}{T_i \rho_{ti}} \right|^2 \right\rangle, \tag{4}$$

the amplitude of the averaged zonal flow potential,

$$\mathcal{Z}^{\frac{1}{2}} \equiv \left[\frac{1}{2} \sum_{k_x} \left\langle \left| \frac{e\phi_{k_x,0}R_0}{T_i \rho_{ti}} \right|^2 \right\rangle \right]^{\frac{1}{2}}, \tag{5}$$

and the ion heat diffusivity in the gyro-Bohm unit χ_i/χ_i^{GB} with $\chi_i^{GB} = \rho_{ti}^2 v_{ti}/R_0$. Therefore, $\mathcal{T}$ and $\mathcal{Z}$ are given by the
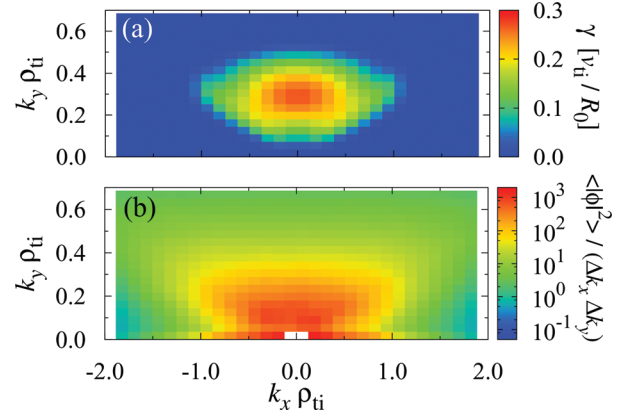

FIG. 7. Two-dimensional spectra for (a) growth rate of linear ITG mode and (b) potential fluctuations (the magnification of the fourth plot of Fig. 6) at $\rho = 0.65$ in the inward-shifted case.

integrations of the spectra of Figs. 8(a) over each wavenumber which are correlated with the linear properties as discussed in the previous section. In the $\mathcal{Z}^{1/2} - \mathcal{T}$ space of Fig. 9(a), all plots in the experimental cases seem to be fitted by a simple proportional relation of $\mathcal{Z}^{1/2} \propto \mathcal{T}$. On the other hand, the result of the inward-shifted case shows the highest ratio of $\mathcal{Z}^{1/2}$ to $\mathcal{T}$ which implies that the zonal flow components are efficiently generated because of the higher zonal flow response in the inward-shifted or neoclassically optimized configuration.[3] It is seen from the plots in $(\chi_i/\chi_i^{GB}) - \mathcal{T}$ space of Fig. 9(b) that the transport level is not simply related to the potential fluctuations or the mixing length estimate shown in Figs. 5(a) and 5(b). On the other hand, one finds in the $(\chi_i/\chi_i^{GB}) - (\mathcal{T}/\mathcal{Z}^{1/2})$ space of Fig. 9(c) that all plots including the inward-shifted case are well represented by the relation,

$$\frac{\chi_i}{\chi_i^{GB}} \propto \frac{\mathcal{T}}{\mathcal{Z}^{\frac{1}{2}}}, \tag{6}$$

despite the fact that a wide range of conditions for the different radial positions and the inward-shifted case are included here. In fact, more than 80% of the data points in the saturation phase are confined in the region surrounded by two lines, $\chi_i/\chi_i^{GB} = C\mathcal{T}/\mathcal{Z}^{1/2}$ with $C = (2.75 \pm 0.75) \times 10^{-1}$. We expect that this relation can be used for modeling of the turbulent ion heat diffusivity applicable to the transport code analyses by estimating $\mathcal{T}$ and $\mathcal{Z}$ from the linear calculation results which include effects of equilibrium profiles and magnetic configurations. Since Eq. (6) is derived from only a limited number of simulation results, we still need to examine many cases with different equilibrium conditions and other physical mechanisms such as the kinetic electron dynamics, which remain as future tasks.

IV. SUMMARY

We have presented the first results of direct comparison between the gyrokinetic ITG turbulence simulations and the experimental observations in the high ion temperature LHD plasma. The present GKV-X simulations, which include full
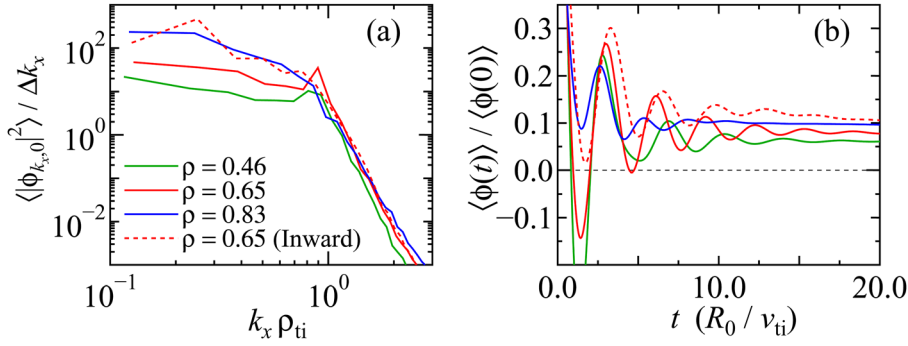
FIG. 8. (a) Spectra of time averages of squared zonal flow potentials in k_x space, and (b) linear responses of zonal flow potentials at $\rho = 0.46$, 0.65, and 0.83 in the experimental case, and at $\rho = 0.65$ in the inward-shifted case. In (a), ϕ and Δk_x are normalized by $T_i \rho_{ti}/eR_0$ and ρ_{ti}^{-1}, respectively. The radial wavenumbers used here are $k_x \rho_{ti} = 0.231, 0.256, 0.244$, and 0.251 for $\rho = 0.46, 0.65$, and 0.83 in the experimental case, and at $\rho = 0.65$ in the inward-shifted case, respectively.

geometry data of the LHD configuration, reproduce the turbulent ion heat fluxes obtained from the experiment within errors of about 30%. The ITG turbulence simulations also have shown the poloidal wavenumber spectrum of the potential fluctuation which is similar to that of the density fluctuation given by PCI measurements in the LHD except for experimentally ambiguous low wavenumber regions. While we still need to improve the GKV-X code by including other effects such as kinetic electrons and electromagnetic fluctuations, the first comparisons of the simulation code with the high-T_i LHD experiment, where the electron density profile is so flattened that the trapped electron mode is considered to be stabilized, have been successfully done and encourages us to confirm that we are on the right track toward more accurate predictions of the anomalous transport in the LHD experiments and future helical reactors based on the gyrokinetic simulations.

The present simulations also verify the spectral transfer of the potential fluctuation into the less-unstable high-k_x region and consequently cause the regulation of turbulent transport. The zonal flows, which are more efficiently generated by the neoclassical optimized configuration, are considered to induce the spectral transfer via the nonlinear entropy transfer.[29] The same analyses as in Ref. [29], which are not demonstrated in the present paper, can be done to directly show the effects of the zonal flows on the spectral transfer in the k_x direction. Detailed results of the spectral transfer analyses will be reported in a separate work.

The simple relation obtained from the simulations, which describes the strong correlation between the turbulent heat diffusivity and the ratio of the squared turbulent potential to the zonal flow amplitude at least within the cases considered in the present work, will be investigated further for use in modeling the ITG turbulent transport in helical plasmas.
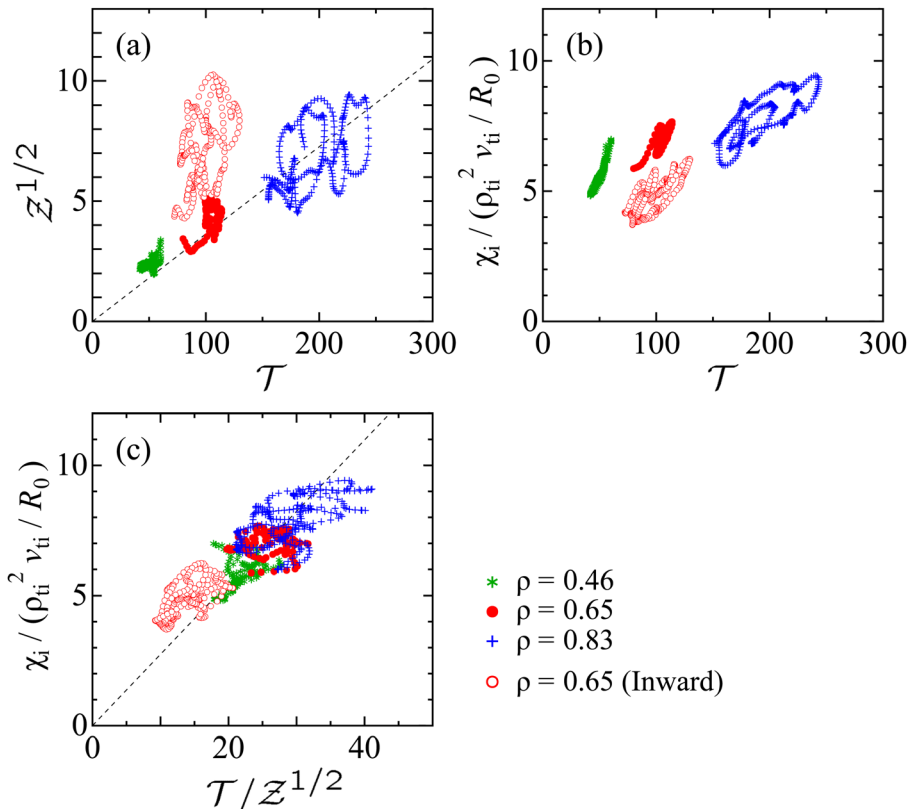

FIG. 9. Lissajous plots of the ITG turbulence simulations of the saturated phases in (a) $(\mathcal{T}, \mathcal{Z}^{1/2})$-space, in (b) $(\mathcal{T}, \chi_i/\chi_i^{GB})$-space, and in (c) $(\mathcal{T}/\mathcal{Z}^{1/2}, \chi_i/\chi_i^{GB})$-space for the experimental cases at $\rho = 0.46, 0.65$ and 0.83, and the inward-shifted LHD case at $\rho = 0.65$, where $\chi_i^{GB} = \rho_{ti}^2 v_{ti}/R_0$ is the gyro-Bohm ion heat diffusivity. Dashed lines in (a) and (c) represent $\mathcal{Z}^{1/2} = \lambda \mathcal{T}$ with $\lambda = 3.63 \times 10^{-2}$ and $\chi_i/\chi_i^{GB} = C\mathcal{T}/\mathcal{Z}^{1/2}$ with $C = 2.75 \times 10^{-1}$, respectively. Here, $\mathcal{T} \equiv (1/2)\sum_{k_x,k_y \neq 0}\langle|\phi_{k_x,k_y}|^2\rangle$ and $\mathcal{Z} \equiv (1/2)\sum_{k_x}\langle|\phi_{k_x,0}|^2\rangle$, where ϕ is normalized by $T_i\rho_{ti}/eR_0$.

ACKNOWLEDGMENTS

[1]M. Wakatani, *Stellarator and Heliotron Devices* (Oxford University Press, 1998).
[2]S. Murakami *et al.*, Nucl. Fusion **42**, L19 (2002).
[3]T.-H. Watanabe, H. Sugama, and S. Ferrando-Margalet, Phys. Rev. Lett. **100**, 195002 (2008).
[4]H. E. Mynick, N. Pomphrey, and P. Xanthopoulos, Phys. Rev. Lett. **105**, 095004 (2010).
[5]P. H. Diamond, S.-I. Itoh, and K. Itoh, *Modern Plasma Physics* (Cambridge University Press, 2010), Vol. 1.
[6]P. H. Diamond *et al.*, Plasma Phys. Controlled Fusion **47**, R35 (2005).
[7]C. Hidalgo, Plasma Phys. Controlled Fusion **53**, 074003 (2011).
[8]A. M. Dimits *et al.*, Phys. Plasmas **7**, 969 (2000).
[9]X. Garbet *et al.*, Nucl. Fusion **50**, 043002 (2010).
[10]T.-H. Watanabe, H. Sugama, and S. Ferrando-Margalet, Nucl. Fusion **47**, 1383 (2007).
[11]P. Xanthopoulos *et al.*, Phys. Rev. Lett. **99**, 035002 (2007).
[12]T. L. Rhodes *et al.*, Nucl. Fusion **51**, 063022 (2011).
[13]A. Komori *et al.*, Fusion Sci. Technol. **58**, 1 (2010).
[14]K. Tanaka *et al.*, Rev. Sci. Instrum. **79**, 10E702 (2008).
[15]K. Tanaka *et al.*, Plasma Fusion Res. **5**, S2053 (2010).
[16]M. Nunami *et al.*, Plasma Fusion Res. **6**, 1403001 (2011).
[17]M. Nunami *et al.*, Plasma Fusion Res. **5**, 016 (2010).
[18]S. P. Hirshman and O. Betancourt, J. Comput. Phys. **96**, 99 (1991).
[19]T.-H. Watanabe and H. Sugama, Nucl. Fusion **46**, 24 (2006).
[20]E. A. Frieman and L. Chen, Phys. Fluids **25**, 502 (1982).
[21]M. A. Beer, S. C. Cowley, and G. W. Hammett, Phys. Plasmas **2**, 2687 (1995).
[22]A. H. Boozer, Phys. Fluids **11**, 904 (1980).
[23]C. D. Beidler and W. N. G. Hitchon, Plasma Phys. Controlled Fusion **36**, 317 (1994).
[24]H. Sugama and T.-H. Watanabe, Phys. Plasmas **13**, 012501 (2006).
[25]P. Helander *et al.*, Plasma Phys. Controlled Fusion **53**, 054006 (2011).
[26]H. E. Mynick and A. H. Boozer, Phys. Plasmas **14**, 072507 (2007).
[27]P. Xanthopoulos *et al.*, Phys. Rev. Lett. **107**, 245002 (2011).
[28]J. Wesson, *Tokamaks*, 2nd ed. (Oxford University Press, 1997), pp. 198.
[29]M. Nakata, T.-H. Watanabe, and H. Sugama, Phys. Plasmas **19**, 022303 (2012).